Monsoon low pressure system like variability in an idealized moist model

Spencer K. Clark*

Program in Atmospheric and Oceanic Sciences, Princeton University, Princeton, New Jersey

Yi Ming

Geophysical Fluid Dynamics Laboratory/NOAA, Princeton, New Jersey

Ángel F. Adames

Department of Climate and Space Science and Engineering, University of Michigan, Ann Arbor, Michigan

**Corresponding author address:* Program in Atmospheric and Oceanic Sciences, Princeton University, 219 Sayre Hall 300 Forrestal Road, Princeton, NJ, USA.

E-mail: skclark@princeton.edu

ABSTRACT

Through a hierarchy of simulations, it is shown that westward-propagating monsoon low pressure system-like disturbances in the Indian monsoon region can be simulated in an idealized moist general circulation model through the addition of a simplified parameterization of land. Three simulations are performed: an aquaplanet case with a slab ocean depth of 20 m, a case with land with realistic continental geometry but no topography, and a case with land and realistic topography. Here land is parameterized as having one-tenth the heat capacity of the surrounding slab ocean, with evaporation limited by a bucket hydrology model. It is found that the prominent topography of the Tibetan Plateau does not seem to be necessary for these storm systems to form or propagate; therefore focus is placed on the simulation with land but no topography. The properties of the storms simulated are elucidated using regression analysis and compared to results from composites of storms from comprehensive GCMs in prior literature. The storms share a similar vertical profile in anomalous Ertel potential vorticity to those in reanalysis, which tilts slightly with the mean easterly vertical zonal wind shear. Propagation, however, does not seem to be strongly dictated by beta-drift. Rather, it seems to be more closely consistent with linear moisture vortex instability theory, with the exception of the importance of nonlinear horizontal moisture advection in the column moisture budget. The results presented here suggest that a simplified GCM configuration might be able to be used to gain a clearer understanding of the sensitivity of monsoon low pressure systems to changes in the mean state climate.

1. Introduction

Southeast Asia has a monsoonal climate. It receives 50 % to 70 % of its annual precipitation during the months of June, July, and August (Neelin 2007). During these months, moisture and dry static energy are abundant, fueling low pressure systems (MLPSs) which originate in the Bay of Bengal and propagate westward against the direction of the prevailing mean low-level winds, across the India at speeds of around $4\,\mathrm{m\,s^{-1}}$ (Adames and Ming 2018b). In May, June, July, August, and September, roughly 80% of all precipitation in this region falls within 1000 km of these lows (Hurley and Boos 2015). For that reason, understanding what influences the propagation and structure of these transient phenomena is important for understanding what controls precipitation during the summer in Southeast Asia.

The growth, propagation, and structure of these low pressure systems has been an area of research for several decades, dating back to Godbole (1977) and references therein. In recent years effort has been made by multiple independent research groups to compile detailed track information for monsoonal disturbances (Hurley and Boos 2015; Hunt et al. 2016a). This effort has led to new insights resulting from rigorous analysis of the composite properties of these storms (Hurley and Boos 2015; Boos et al. 2015; Ditchek et al. 2016; Hunt et al. 2016a,b; Cohen and Boos 2016; Sandeep et al. 2018). In particular, early theoretical attempts to explain the growth and propagation of monsoon depressions in terms of barotropic (Shukla 1977; Lindzen et al. 1983), baroclinic (Mishra and Salvekar 1980; Mak 1983; Moorthi and Arakawa 1985), or combined barotropic-baroclinic (Krishnamurti et al. 1976a; Shukla 1978) instability mechanisms have recently been challenged by a number of alternative ideas.

The motivation to search for alternative explanations can be traced in part back to Cohen and Boos (2016). They investigated composites of observed monsoon depressions in reanalysis and compared them with the canonical example of moist baroclinic instability: diabatic Rossby waves in the mid-latitudes. They found that in monsoon depressions, anomalies in Ertel potential vorticity do not tilt against the mean vertical wind shear as they do in diabatic Rossby waves, which they argue is evidence against moist baroclinic instability operating as a mechanism in fueling the growth of the disturbances. In the paper they also argue, based on prior literature (Krishnamurti et al. 1976b, 2013), that barotropic instability plays a minor, if any, role in the development of MLPSs.

In the last five years, four, possibly overlapping, alternative explanations for monsoonal disturbance propagation have been proposed. The first is that monsoon depressions might be better described as tropical-cyclone-like features propagating via adiabatic beta drift (Boos et al. 2015). Another possible explanation, proposed in Hunt and Parker (2016), is that the Himalayan mountains may act as a rigid northern meridional boundary in the lower troposphere, leading to westward propagation of a cyclonic vortex to the south via an effective mirror-image vortex. Adames and Ming (2018a) develop a linear theory for monsoonal disturbances within a mid-latitude moisture-mode like framework, which suggests that properties of the disturbances, like their phase speed and preferred horizontal scale, may be sensitive to properties of the mean state climate like the mean meridional temperature and moisture gradients. Finally, Diaz and Boos (2018) revisit the potential influence of barotropic instability, and find that even in the absence of convective heating, growing disturbances fueled by barotropic instability could be possible with a zonally-uniform basic state. These theories are still young, and their utility for explaining the properties of monsoonal disturbances and their potential sensitivity to changes in the mean state (e.g. induced by increasing greenhouse gas concentrations) has yet to be extensively investigated.

The complications of the real world, however, make monsoonal disturbances difficult to study. For instance many comprehensive general circulation models used in the CMIP5 archive struggle to obtain a realistic distribution of climatological mean JJAS precipitation rate in the Indian monsoon region (see the supplement of Sandeep et al. 2018). In addition, several models from the AMIP archive simulate unrealistic patterns of synoptic activity index (SAI) (see the supplement of Sandeep et al. 2018), a metric that quantifies an intensity-weighted frequency of monsoon low pressure system days per season at each location (Ajayamohan et al. 2010). To some extent these errors are attributed to the coarse horizontal resolution of these models; indeed studies have shown that models run with higher resolution such as the UK Met Office's Unified Model or GFDL's Hi-RAM demonstrate increased skill in simulating MLPSs (Hunt and Turner 2017; Sandeep et al. 2018).

Despite sometimes having errors in the exact location of storms, however, some coarse-resolution GCMs (such as GFDL's AM4) have been shown to have the ability to reasonably simulate their general frequency statistics and structure (Adames and Ming 2018b), indicating that exact-realism of precipitation location and mean winds is not necessarily required for studying the structure and propagation of these dynamical phenomena. It prompts the question of whether a simpler model, lower in the complexity hierarchy, could capture the essence of monsoon low pressure systems. By a simpler model, we mean one somewhere in between an idealized aquaplanet GCM (like Frierson et al. 2006) and a comprehensive GCM (complete with intricate parameterizations of convection, clouds, radiation, land, chemistry etc.).

In order to approximately simulate a monsoon climate (with mean summertime easterly wind shear and tropical precipitation displaced far from the equator), one must provide some mechanism for a locally poleward-increasing meridional temperature gradient to develop in the subtropics (this follows from thermal wind balance). The most natural way of doing this is to add a simple treatment of land, poleward of the equator, to an idealized aquaplanet GCM, with a lower heat capacity than the surrounding ocean; in the summer, the land will heat faster than the surrounding ocean, resulting in the desired effect. This type of approach has already been used to study aspects of mean state monsoon circulations in a number of studies (e.g. Merlis et al. 2012b; Maroon et al. 2016; Maroon and Frierson 2016; Voigt et al. 2016; Geen et al. 2017; Zhou and Xie 2018).

To date, however, the behavior of transient disturbances in these types of idealized simulations/models has not been frequently addressed. Given the models' often low-horizontal-resolution nature, and crude treatments of convection, one perhaps might not expect realistic tropical variability. That being said, while their occurrence was attributed to baroclinic instability based on classical monsoon literature, Xie and Saiki (1999) found abundant westward-propagating cyclonic vorticity anomalies (akin to monsoon low pressure systems) in a simulation using a very low horizontal resolution GCM (T21 spectral truncation) with heavily simplified lower boundary conditions meant to crudely mimic the Asian monsoon region. It is worth revisiting these disturbances in a similar setup in light of recent developments (e.g. Boos et al. 2015; Cohen and Boos 2016; Hunt and Parker 2016; Adames and Ming 2018a,b), to see if they in fact are dynamically similar phenomena to those seen in the real world and comprehensive GCMs (i.e. not manifestations of baroclinic instability).

In this study we will start from a version of Frierson et al. (2006)'s idealized moist model coupled to a full radiative transfer code (Clark et al. 2018), and slowly build up in complexity to attain an environment capable of supporting monsoon low pressure system-like disturbances. We will use this setup, coupled with rigorous analysis of the composite anomalous budgets of Ertel potential vorticity, vorticity, column internal energy, column water vapor, and column moist static energy, to discuss the potential applicability of the theories for MLPS propagation described above, and touch on the importance of various boundary conditions (like topography) in the realism of the disturbances simulated.

2. Methods

a. Model description

The modeling setup we use to simulate monsoon low pressure systems is heavily idealized. Our starting point is the Geophsyical Fluid Dynamics Laboratory (GFDL) idealized moist model as configured in Clark et al. (2018). This model was first introduced in Frierson et al. (2006, 2007), where it consisted of a spectral dynamical core, with simplified moist physics, boundary layer, and radiation parameterizations. It has since been modified to add a simplified Betts-Miller moist convection scheme (Frierson 2007), alterations to the boundary layer scheme (O'Gorman and Schneider 2008), and an option to run with full radiative transfer, rather than the original gray radiative transfer scheme (Clark et al. 2018). While the full radiative transfer scheme interacts with the active water vapor tracer in the model, there is no parameterization of cloud condensate, and therefore no cloud radiative effects or feedbacks. Slab ocean aquaplanet configurations similar to this (i.e. full radiative transfer with simplified moist physics) have been used before, e.g. in Merlis et al. (2012a,b), Jucker and Gerber (2017), and Vallis et al. (2018).

In this study, we seek to examine monsoon low pressure systems in the South Asia region. Due to the annual cycle in solar insolation, these occur in the boreal summer months of June, July, August, and September. To capture this seasonal variation in climate, we run all of our simulations with Earth's current approximate obliquity and eccentricity parameters, 23.439° and 0.01671 respectively. In addition, in some experiments we introduce a crude parameterization of land. In prior studies, land has been added to variants of this model with varying degrees of complexity depending on the application, typically involving modification of some combination of the heat capacity, the evaporation parameterization, the surface roughness, the surface albedo, and surface height over the land portion of the domain (e.g. Byrne and O'Gorman 2012; Merlis et al. 2012b; Maroon et al. 2016; Maroon and Frierson 2016; Voigt et al. 2016; Geen et al. 2017; Vallis et al. 2018; Zhou and Xie 2018). In other models, simplified land has been added in similar ways (e.g. Xie and Saiki 1999; Becker and Stevens 2014; Cronin et al. 2015). As a starting point in our model we choose to distinguish land from the default lower boundary, a slab ocean, in only two ways: its heat capacity, and its treatment of evaporation.

The land setup maintains the slab ocean model across the entire lower boundary; however, over land grid cells we use a shallower mixed layer depth (which controls the heat capacity) and scale the potential evaporation rate as predicted by the bulk formula over a saturated surface by a fraction determined using a simple bucket hydrology model [the same as described in Vallis et al. (2018), which is similar to that in Byrne and O'Gorman (2012) or Zhou and Xie (2018), which dates back to Manabe (1969)]. The mixed layer depths over land and ocean are the same as those used in experiments in Geen et al. (2017) (2 m over land and 20 m over ocean) and the bucket hydrology model parameters are the same as those described in Vallis et al. (2018) (a bucket depth of 150 mm and a bucket saturation fraction of 0.75). By default we supply the model with no topography and use a surface albedo of 0.26 over land and ocean. The global mean surface albedo is greater than it might be in a comprehensive GCM due to the lack of clouds in this model (Frierson et al. 2006). Finally, we prescribe zero ocean heat flux in our simulations; in other words we assume the ocean does not facilitate any horizontal energy transport.

While we idealize what constitutes the land surface in the model, we opt not to idealize land geometry. In all of our experiments we prescribe realistic present-day continental shapes. We use approximately present-day concentrations of the well-mixed greenhouse gases (CO_2 = 369.4 ppm, CH_4 = 1.821 ppm), and prescribe a hemispherically-symmetric pattern of ozone, based on the Aqua-Planet Model Intercomparison Project (Blackburn et al. 2013).

Similar to Geen et al. (2017), to improve the numerical stability of the dynamical core in the upper levels of the model, we add a Rayleigh damping tendency to the horizontal winds. The Rayleigh damping coefficient we use decreases from a value near $0.33\,\mathrm{d}^{-1}$ at the top of the model to near zero near the surface, following the vertical profile defined in Equations 13.89 and 13.90 in Jablonowski and Williamson (2011), which were first used in Boville (1986). This Rayleigh damping profile was used for several years in the European Centre for Medium-Range Weather Forecasts (ECMWF) Integrated Forecast System (IFS) model (Jablonowski and Williamson 2011).

b. Experiments

To test the idealized moist model's ability to simulate monsoon low pressure systems, we first conduct simulations with varying levels of land-complexity, with the goal of finding a minimal configuration that approximately captures their observed characteristics, e.g. their timing during the year, frequency, intensity, location, and speed/direction of propagation. We run all our cases for 20 years, starting from spatially-uniform initial conditions (constant initial temperature and specific humidity), storing 6-hourly mean values of relevant diagnostics. After the first 10 years, the model approximately reaches equilibrium; therefore we use the final ten years of the simulation for analysis. All cases are run with 40 unevenly-spaced vertical sigma levels, and at T42 spectral resolution, approximately $2.8^\circ \times 2.8^\circ$ horizontal resolution.

For illustration, we will show the results of three experiments to start out. The three experiments we will discuss here are a simple aquaplanet simulation with a mixed layer depth of $20\,\mathrm{m}$ everywhere (referred to as the AQUA case), a simulation with "land" as described above with flat topography (referred to as the LAND simulation), and a simulation with "land" and realistic spectrally-smoothed topography, as in Lindberg and Broccoli (1996), (referred to as the TOPO simulation). We will show that the LAND simulation has adequate boundary conditions to simulate monsoon low pressure system-like storms in the Indian monsoon region during June, July, August, and September, while the AQUA simulation is too simple effectively simulate these transient disturbances, and the additional complexity of the TOPO simulation is not necessarily needed. For that reason, for most the manuscript, we will focus on the results of the LAND case.

c. Analysis techniques

To analyze the structure of monsoon low pressure systems in our model, we employ frequency-wavenumber spectral analysis and compute lag regression patterns. Frequency-wavenumber spectral analysis allows us to identify the frequencies and wavenumbers of the zonally-propagating waves that are most prevalent; this type of analysis was popularized in Wheeler and Kiladis (1999) and Hendon and Wheeler (2008). Lag regression patterns allow us to determine the spatial structure of variable anomalies projected onto a monsoon low pressure system index. We approximately follow the methods described in Adames and Ming (2018b). Here we will explain the details of these techniques which we will employ later.

To compute frequency-wavenumber power spectra, we start with 6-hourly resolution model output of the precipitation rate. We then subset this dataset in time such that it only includes datapoints for the months June, July, August, and September. From this timeseries, we construct a set of 60-day segments, which overlap by 30 days, generating a four-dimensional dataset (time, longitude, segment, latitude). We apply a Hanning window over the time dimension, tapering the endpoints of the segments toward zero to minimize spectral leakage (Welch 1967); in addition, we apply a Hanning window over 50°E to 130°E to taper data to zero outside our longitudinal region of interest. After this preparation, we compute a fast Fourier transform (FFT) in longitude and time, and compute the power as the square of the magnitude of the complex Fourier coefficients. To construct a two-dimensional frequency-wavenumber diagram, we average the power over the segments and between latitudes bounding the region of interest for the particular dataset, which correspond roughly to the latitudinal bounds of the South Asian monsoon region, and then compare it to a reference red frequency spectrum. We define the region of interest for a particular dataset as $\pm 5°$ from the latitude of maximum mean JJAS precipitation rate[1] along the 80°E longitude band. We compute the red spectrum as in Masunaga et al. (2006), normalizing such that the sum of the power in non-zero frequencies matches that in the power spectrum of the precipitation rate.

To compare the power in the signal to that in the reference red spectrum, we compute what is referred to as the "signal strength" by determining the ratio of the difference between the power spectrum (P) and red spectrum (R) to the power spectrum itself:

$$S = \frac{P - R}{P}. \tag{1}$$

Statistical significance is determined by computing a critical value of a chi-squared-statistic at the 99% significance level, which compares the ratio of two variances scaled by the degrees of freedom minus one, e.g. $\chi^2 = \frac{P(n-1)}{R}$, where n is the number of degrees of freedom. The number of degrees of freedom used in computing the critical chi-squared value is calculated as in Hendon and Wheeler (2008) and Adames and Ming (2018a); it is equal to 2 (amplitude and phase) x 10 (number of years) x 122 (number of days in JJAS per year) / 60 (days per segment) ≈ 40. At the 99% level, this results in a value of 62.4, indicating that if the power of the signal is 1.6 times that of the red spectrum then there is a 1% chance the signal emerged out of red noise. In terms of the signal strength (in Equation 1), this means in order for the signal to be statistically-significant at the 99% level, the signal strength must be greater than or equal to approximately 0.38.

[1]Hurley and Boos (2015) note that monsoon low pressure system activity is strongest slightly poleward of this maximum in most monsoon regions; however we claim that as a first approximation this is a reasonable method of defining the central latitude of our region of interest.

To compute lag regression patterns we follow the methods of Adames and Wallace (2014) and Adames and Ming (2018b). This requires computing an index, which measures the intensity of monsoon low pressure system activity. Adames and Ming (2018b) do this spectrally filtering the precipitation rate to include wave activity from only monsoon low pressure system like modes ($-25 \leq k \leq -3$; $f \geq 0.067\,\mathrm{d}^{-1}$), then averaging over the spatial region of interest (here defined as $\pm\,5°$ latitude from the latitude of maximum JJAS mean precipitation rate, between 75°E and 85°E in longitude); this results in a one-dimensional index over time, which is then standardized such that it has a mean of zero and a standard deviation of one. Here k is the non-dimensional zonal wavenumber, which can be related to a dimensional zonal wavenumber $\tilde{k}$ via $k = \tilde{k}a\cos\phi$, where a is the radius of the Earth and ϕ is latitude, and f corresponds to the frequency of the waves. The spectral filtering is achieved by performing standard Fourier transforms in time and longitude of the raw precipitation rate timeseries, zeroing out all coefficients outside of the rectangular spectral region specified above, and finally computing an inverse Fourier transform back to time and longitude space. With an index in hand, we can then regress any variable against it. Borrowing notation from Adames and Wallace (2014) this looks like:

$$\mathbf{D} = \frac{\mathbf{S}\mathbf{P}^T}{N}. \tag{2}$$

Here $\mathbf{S}$ is a two-dimensional matrix with each row representing the time series of a variable at a given gridcell; $\mathbf{P}$ is the standardized index at each time (i.e. it is a single row vector); N is the number of values in the index; and $\mathbf{D}$ is the computed regression pattern. $\mathbf{D}$ contains a time-independent spatial pattern of anomalies with the same dimensions as the input variable. Lag regressions can be computed by shifting the index forward or backward in time and applying the same procedure, noting that this reduces the number of overlapping elements between the index and variable (i.e. it slightly changes N). This allows us to construct a picture of what the conditions look like before, during, and after a monsoon low pressure system event occurs.

To smooth out regression patterns, particularly in the context of the tracer budgets, we apply a similar regression-compositing technique to that was employed in Adames and Ming (2018b). This entails computing regression patterns for index regions shifted -2, -1, 0, 1, or 2 grid cells away in longitude and/or latitude from the original center of the region of interest described above, and then shifting the regression patterns back to all be centered at the same location and averaging. This results in computing and taking the mean of 25 regression patterns, producing a smoother picture.

3. Mean state climate in the simulation hierarchy

Speaking broadly, there are a number of distinctive attributes of the mean state climate in the Asian monsoon region during June, July, August, and September (JJAS). These attributes are a local maximum in mean precipitation rate, meridionally-increasing temperature and moisture gradients, and surface westerly and upper-level easterly winds (i.e. "easterly shear", with winds becoming more easterly with height) (Sikka 1977). Here we will discuss the mean state climate of the AQUA, LAND, and TOPO simulations with respect to these attributes.

The simplest configuration is an aquaplanet with a 20 m mixed layer depth everywhere (the AQUA simulation); in this case, the annual cycle of precipitation is significantly lagged from that on Earth's, with monthly mean precipitation rates maximizing during September and October in the latitudes of the Asian monsoon region (not shown). Not only that, the temperature gradients and wind shear are in the wrong direction [meridionally-decreasing and weakly westerly, respectively, Figure 1(d) and (g)]. Therefore it is not a good simulation to look for realistic monsoon low pressure system like disturbances.

Moving on to the LAND simulation, we see an improvement. The JJAS mean precipitation rate in the Asian monsoon region for the LAND simulation is plotted in Figure 1(b). We can see two rain bands, one centered near the equator, and one centered around 12.6°N. This sort of double-ITCZ structure was also found in Xie and Saiki (1999); in their idealized simulation they also found latitudinal maxima in summer precipitation in the Asian monsoon region. To a lesser extent (i.e. the local maximum in precipitation is substantially weaker near the equator) it is also seen after monsoon onset in the idealized "flat" simulation of Geen et al. (2017), which uses a similarly-configured model as to our LAND simulation, with the one exception being the addition of AMIP-derived slab ocean heat fluxes in their case. In general, when compared with observations, significant fine-scale spatial structure is lacking due to the low resolution nature of the simulation and lack of topography. That said, in a broad sense, the LAND case captures the significant local northward migration of the intertropical convergence zone (ITCZ) in this region during this time period, with the ITCZ at other longitudes (e.g. in the Pacific Ocean) remaining closer to the equator.

A notable feature in reanalysis data is that column integrated moisture increases steadily as one moves northward from the equator through the Bay of Bengal (Adames and Ming 2018b). This strong positive meridional moisture gradient has been theorized to play a role in the dynamics of monsoon low pressure systems (Adames and Ming 2018a). Panel (e) Figure 1 shows the JJAS mean column integrated moisture in the LAND simulation. There we can see a band of high column integrated water vapor roughly coincident with the band of high precipitation rate, running from the Arabian Sea, across India, and over the northern Bay of Bengal and Southeast Asia. When compared with reanalysis, this local maximum in column water vapor over the Bay of Bengal is displaced slightly southward (in reanalysis the maximum is located closer to the land-sea boundary between Bangladesh and the Bay of Bengal). In addition, column integrated moisture magnitudes are substantially smaller than those seen in reanalysis, with maximum values of around 20 mm in our idealized simulation and around 60 mm in reanalysis (Adames and Ming 2018b).

Finally, another important property of the mean state Asian monsoon climate is a meridionally-increasing surface temperature field, and attendant easterly vertical wind shear, with westerly winds near the surface and easterly winds aloft (Xie and Saiki 1999; Boos et al. 2015; Cohen and Boos 2016). The meridionally-increasing temperature gradient is induced by the difference in heat capacity between the land and ocean. Because the land heats up faster than the ocean, it experiences greater seasonal variation in surface temperatures than ocean at similar latitudes. In the summer the southern portion of the Asian continent is warmer than the Indian Ocean. Our crude setup in the LAND simulation is able to capture this, as indicated in Figure 1(h). There the vectors represent the magnitude and direction of the JJAS mean vertical wind shear, as computed in Boos et al. (2015) as the difference in horizontal winds between the 200 hPa and 850 hPa pressure levels. The mean shear is predominantly easterly, with strongest values of about 30 $\mathrm{m\,s^{-1}}$ at around 12.5°N, which is similar to that seen in reanalysis. In addition, the magnitude of the shear decreases as one moves northward over the Asian continent, which is also consistent with the real world (Boos et al. 2015).

Adding more realism to the model in the form of realistic topography in the TOPO simulation makes some aspects of the simulated the climate more realistic (e.g. column water vapor maximizes farther north near the shore of the Bay of Bengal); however despite spectrally regularizing the relief pattern to minimize Gibbs ripples as in Lindberg and Broccoli (1996) we find that in the Asian monsoon region significant unrealistic ripples in the mean JJAS precipitation pattern south of the Tibetan Plateau [Figure 1(c)] complicate analysis and do not provide any added realism as it pertains to monsoon low pressure systems. These ripples can also be seen an analogous simulation conducted in Geen et al. (2017) [see their Figure 11(h)]. Therefore in the remainder of the manuscript we will focus our attention on analyzing the detailed structure and properties of the storms obtained in the simpler LAND simulation with no topography. We leave further possible idealization of the continental geometry and evaporation parameterization to future work.

4. The character of Indian monsoon low pressure systems in the LAND simulation

a. Frequency-wavenumber power spectrum

Despite the simplicity of the setup of the LAND simulation (notably omitting the impacts of the prominent land surface topography of Southern Asia, and the impacts of ocean heat transport), we seem to obtain an adequate JJAS mean state climate to support westward-propagating, precipitation-inducing disturbances. We can see this clearly in looking at a frequency-wavenumber power spectrum of the precipitation rate averaged between the latitudes 7.6°N and 17.6°N in the LAND simulation (Figure 2). There we find statistically-significant signal strength between zonal wavenumbers -20 to -5, and frequencies $0.10\,\mathrm{d}^{-1}$ to $0.35\,\mathrm{d}^{-1}$. This pattern in signal strength is largely consistent with that seen in daily precipitation rate observations from the Tropical Rainfall Measurement Mission (TRMM) (Huffman et al. 2007) and simulations using GFDL's AM4 (Adames and Ming 2018b)[2], which is indicative of westward-propagating waves of alternating wet and dry periods with a horizontal scale on the order of 1000 km and a period of around 3 d to 10 d.

b. Horizontal structure of the precipitation and low-level wind anomalies

The structure of these disturbances can be elucidated using regression analysis as described in Section 2c, following the methods of Adames and Ming (2018b). We will first consider the

[2]Note that the region of interest used in Adames and Ming (2018b) for the observations and AM4 was centered at 17.5°N, rather than at 12.6°N in the case of the LAND experiment in Figure 2.

horizontal structure of the anomalous precipitation and low-level (850 hPa) wind fields on days preceding, during, and after a storm event centered at 80°E and the latitude of maximum mean JJAS precipitation along 80°E in the South Asian monsoon region. In the LAND simulation, as we look at the lag sequence descending from the top of Figure 3, we can see clear evidence of a westward-propagating cyclonic disturbance crossing the Bay of Bengal and traversing of India over a span of about 5 days. The disturbance is flanked by dry anticyclonic circulations. The maximum wind speed anomaly associated with the regression in the LAND experiment at lag day zero is $2.2\,\mathrm{m\,s^{-1}}$. While this might seem relatively weak, particularly when compared with monsoon depressions, which have wind speeds over $8.5\,\mathrm{m\,s^{-1}}$ (Hurley and Boos 2015), we must note that the anomalies obtained via regression analysis represent a composite of sorts; this does not necessarily mean that stronger storms (of the magnitude of monsoon depressions) do not occur in the LAND simulation[3].

In comparison to regression results from GFDL's AM4, the disturbances are located farther south, have weaker precipitation anomalies (on the order of $4\,\mathrm{mm\,d^{-1}}$ versus $10\,\mathrm{mm\,d^{-1}}$), but similar magnitude wind anomalies. The propagation direction is almost directly westward, the same direction as the climatological vertical wind shear [Figure 1(h)], raising the possibility that the disturbances could be adiabatically advected by the climatological mid-tropospheric winds (Boos et al. 2015).

The propagation velocity of the storms can be quantified by computing the location of the centroid of the positive precipitation anomalies at each lag day. This is done by separately taking weighted means of the longitude (λ) and latitude (ϕ), with the positive precipitation anomalies

[3]In fact, if we compute composite means of the anomaly patterns associated with precipitation index values greater than two (approximately the strongest 3-4% of storms), we find storm-center precipitation anomalies on the order of $10\,\mathrm{mm\,d^{-1}}$, maximum wind speed anomalies near $8.5\,\mathrm{m\,s^{-1}}$, and minimum surface pressure anomalies of less than 3.6 hPa (not shown).

(P') forming the weights:

$$\lambda_0(t) = \frac{\iint_A H\left\{P'\right\} P' \lambda \,\mathrm{d}A}{\iint_A H\left\{P'\right\} P' \,\mathrm{d}A}, \tag{3}$$

$$\phi_0(t) = \frac{\iint_A H\left\{P'\right\} P' \phi \,\mathrm{d}A}{\iint_A H\left\{P'\right\} P' \,\mathrm{d}A}, \tag{4}$$

where H is the Heaviside step function, which takes the value 1 for inputs greater than or equal to 0, and 0 for inputs less than 0, and the area of integration A, is $\pm 5^\circ$ surrounding the latitude of maximum JJAS mean precipitation at 80°E and 50°E to 110°E in longitude. The centroid in each lag day plotted in Figure 3 is marked with a filled black circle. We can compute an average zonal and meridional propagation velocity over the four-day window plotted in Figure 3 for each simulation by taking the difference in the position of the centroid at lag day 2 and the position of the centroid at lag day -2 and dividing by the difference in time (4 d). If we do this, we find that the average zonal propagation velocity of the centroid in the LAND simulation is $-6.2\,\mathrm{m\,s^{-1}}$, while the average meridional propagation velocity is $-0.1\,\mathrm{m\,s^{-1}}$. The propagation velocity in our simulation is stronger and more westward-directed than in reality (Boos et al. 2015) or in comprehensive GCMs (Adames and Ming 2018b); there zonal propagation velocities are typically on the order of $4\,\mathrm{m\,s^{-1}}$ or smaller, and there is a more significant meridional component.

5. Theoretical mechanisms of monsoon low pressure system growth and propagation

As discussed earlier, numerous possible explanations have been suggested for which mechanisms might dictate the growth and propagation of monsoon low pressure systems. Through systematic analysis, we will now investigate the potential role each suggested mechanism might be playing in the storms in our LAND simulation.

a. Baroclinic instability

With certain treatments of moist convection, some theoretical studies have shown that disturbances with the spatial scale and frequency of monsoonal disturbances could be fueled by baroclinic instability in the region of a easterly vertical wind shear (Mishra and Salvekar 1980; Mak 1983; Moorthi and Arakawa 1985). To investigate whether baroclinic instability could be playing a role in the storms in our simulation, we turn to the "tilt-against-the-shear" diagnostic suggested by Cohen and Boos (2016): whether anomalies in Ertel potential vorticity (PV) tilt with or against the mean easterly vertical wind shear. To see if this is the case, we can look at the vertical structure of Ertel PV (EPV) anomalies along a zonal cross section.

We can compute EPV from data interpolated to levels of constant pressure following Bluestein (1992) via:

$$q_d = -\frac{\partial\theta}{\partial p}\left[\frac{1}{a\cos\phi}\left(\frac{\partial\left(v\cos\phi\right)}{\partial\lambda} - \frac{\partial u}{\partial\phi}\right) + f - \frac{R}{\sigma p}\left(\frac{1}{a\cos\phi}\frac{\partial T}{\partial\lambda}\frac{\partial v}{\partial p} - \frac{1}{a}\frac{\partial T}{\partial\phi}\frac{\partial u}{\partial p}\right)\right], \tag{5}$$

where σ is the static stability parameter given by:

$$\sigma = -\frac{RT}{p}\frac{\partial\ln\theta}{\partial p}, \tag{6}$$

and all horizontal derivatives are computed on surfaces of constant pressure. Note we have taken the liberty to convert the expression in Bluestein (1992) from Cartesian to spherical coordinates. u, v, θ, T, p, ζ, f, and R represent the zonal wind, meridional wind, potential temperature, temperature, pressure, vertical component of the relative vorticity, the Coriolis parameter, and the specific gas constant of dry air, respectively. The subscript θ is meant to denote that while we use data on surfaces of constant pressure, the horizontal derivatives are computed such as to be on surfaces of constant potential temperature. We neglect contributions of the horizontal components of the vorticity to the potential vorticity as they were small in Boos et al. (2015) and do not expect things to be materially different here. Horizontal derivatives are computed using second-order centered finite differences following the methods described in Seager and Henderson (2013). Vertical derivatives were computed using second-order centered finite differences in the interior and first order finite differences on the boundaries. We can scale q_d by $10^6 g$ to convert it to potential vorticity units (PVU), where g is the gravitational acceleration.

If we compute EPV using the six-hourly output for each simulation, regress it onto the precipitation index at lag day zero, and average the result of the latitudes of the region of interest, the result is Figure 4(a), a zonal cross-section of anomalous EPV. Overlaid are contours representing a similar cross section of temperature anomalies. At lag day zero there is a fairly upright column of anomalous positive EPV with a maximum in the mid-troposphere. The column of EPV tilts slightly westward with height [in the direction of the shear vector plotted in Figure 1(h)]. The positive EPV anomalies are flanked to the west and east by weaker, also fairly upright, negative EPV anomalies. Above the 200 hPa pressure level in both simulations there are strong positive EPV anomalies slightly to the east of the mid-tropospheric EPV anomalies. It is possible one could interpret these as evidence of tilting against the shear; however, EPV anomalies above the 200 hPa pressure level are not included in the Cohen and Boos (2016) "tilt against the shear" metric. Therefore, we take the anomaly patterns presented here as evidence that baroclinic instability is not playing a role in the life cycle of the low pressure systems simulated in our idealized model.

If we compare the vertical structure of EPV and temperature anomalies in monsoon low pressure systems in the LAND simulation with the structures seen in composites of monsoon depressions from reanalysis midway through the storm lifetime shown in Cohen and Boos (2016) we find some similarities and differences. In reanalysis, monsoon depressions are characterized by a column of anomalous positive EPV, with a width of about 8° longitude, similar to our simulations. There are two local maxima in the vertical in reanalysis (one at around 700 hPa and one at around 500 hPa), whereas there is only one in the idealized model [see around 600 hPa in Figure 4(a)]. The temperature anomaly structure in our simulation is also broadly similar to that seen in reanalysis. As in our case, in reanalysis the disturbances are characterized by positive temperature anomalies in the upper troposphere and negative temperature anomalies in the lower troposphere. In both the temperature anomalies and EPV anomalies there is slight tilt with the shear. Likely owing in part to the fact that Cohen and Boos (2016) look at composites of monsoon depressions (and omit weaker monsoon low pressure systems in their analysis), the anomalies in EPV and temperature we find in our regression analysis are weaker than what they find in reanalysis.

b. Advection by the mean upper-level easterly winds

Setting the question of what leads to low pressure system growth aside for the moment, Boos et al. (2015) suggest that one possible mechanism for the propagation of monsoon depressions would simply be horizontal advection of the mid-tropospheric EPV maximum by the total mean winds. One simple way to test this possibility in our simulation is to look at a meridional cross section (i.e. averaged between 75°E and 85°E) of EPV anomalies computed through regression analysis (rather than a zonal one) in conjunction with a meridional cross section of the JJAS mean zonal winds. This is shown in Figure 4(b). There we find that the climatological zonal wind at the latitude and pressure level of the maximum EPV anomaly is eastward at approximately $2\,\mathrm{m\,s^{-1}}$. This is in contrast to the direction of propagation of the storm center, which is westward. Moreover, in Figure 4(b), while there are less significant portions of the EPV anomaly pattern that do overlap with westward JJAS mean winds in the upper troposphere, these winds have a weaker magnitude than the westward propagation speed of the precipitation anomalies (on the order of $-6\,\mathrm{m\,s^{-1}}$) shown in Figure 3. This suggests that advection of the vortex center by the mean winds cannot explain the overall westward propagation of the storm systems in our simulation and that the propagation must instead be explained by either advection by the anomalous winds or diabatic processes.

c. Beta drift

An alternative explanation for the propagation of monsoon depressions is provided in Boos et al. (2015). There, it is argued that they could propagate in a similar manner to tropical cyclones, via adiabatic beta drift. Boos et al. (2015) base this hypothesis off of a composite analysis of Indian monsoon depressions using tracks and positions from their own archive (Hurley and Boos 2015) and meteorological variables derived from the ERA-Interim reanalysis (Dee et al. 2011). It is found that if the total streamfunction for the horizontal winds at 500 hPa in the composite mean is linearly decomposed into a component that is azimuthally-symmetric about the vortex center and a residual (referred to as the azimuthally-asymmetric component) as in Fiorino and Elsberry (1988) and Wang and Holland (1996), that two "beta gyres" flank the center of the vortex. These beta gyres are thought to form because of the ambient gradient in planetary vorticity (β); on the westward side of a cyclonic circulation, one would expect a positive tendency in vorticity due to the advection of high-vorticity air from the north (resulting in an anomalous cyclonic circulation to the west), while on the eastward side of the cyclonic circulation, one would expect a negative tendency due to the advection of low-vorticity air from the south (resulting in an anomalous anti-cyclonic circulation to the east). The winds from these two anomalous circulations then can advect the storm center in a direction which depends on the orientation of the of the beta gyres. In the case of Boos et al. (2015), the anomalous circulations associated with the beta gyres derived from the composite analysis suggested advection of the storm center to the northwest (consistent with the storms' actual direction of propagation).

The mechanism of beta drift requires advection of anomalous EPV by the anomalous winds generated by the storm. Therefore, we can investigate this possibility in the LAND simulation by computing the anomalous terms in the EPV budget, and eventually decompose the horizontal advection term into components due to linear and nonlinear terms. An equation governing the time tendency of EPV is given in Boos et al. (2015):

$$\left(\frac{\partial q_d}{\partial t}\right)' = \left(\frac{1}{\rho}\eta \cdot \nabla\dot{\theta}\right)' - (\mathbf{u} \cdot \nabla q_d)' - \left(\omega \frac{\partial q_d}{\partial p}\right)'. \tag{7}$$

We compute the terms in the anomalous budget by regressing the time series of each term against the precipitation index we defined earlier. The first term on the right hand side of Equation 7 corresponds to diabatic processes, and the second and third terms correspond with horizontal and vertical advection, respectively. It follows that under adiabatic processes, EPV is conserved following the flow. Rather than compute the diabatic term explicitly, we instead explicitly compute the time tendency of EPV and advection terms, and compute the diabatic term as a residual.

1) The full anomalous EPV budget

Spatial patterns of the different terms for at the 500 hPa and 700 hPa levels are shown in Figure 5. There we find that the pattern of anomalous EPV time tendency [panels (a) and (e)] is consistent with the westward-propagation of the storms, with positive EPV tendencies to the west of the vortex center and negative EPV tendencies to the east at either level. As Boos et al. (2015) found in a case study of a monsoon depression, in the mid-troposphere a negative diabatic tendency at the storm center [Figure 5(b)] is largely compensated for by a positive vertical advection tendency in the same location [Figure 5(d)]. At this level in Boos et al. (2015) and in our simulation, anomalous horizontal advection of EPV [Figure 5(c)] appears to project most strongly onto to the spatial pattern of the overall EPV tendency. Closer to the surface, at 700 hPa, diabatic processes appear to play a larger role in the propagation tendency [cf. Figure 4(d) and Figure 4(e)], with horizontal advection no longer being as significant; again this is similar to what is found in Boos et al. (2015) in reanalysis.

While the results plotted in Figure 5 provide qualitative evidence of the importance of horizontal advection and diabatic processes in the propagation of EPV anomalies, we can be more quantitative about this assessment by using projection a technique that has been used in a number of studies seeking to quantify the importance of terms to an overall budget of a quantity, e.g. $\frac{\partial q_d}{\partial t}$ (e.g. Andersen and Kuang 2011; Lutsko 2017; Adames and Ming 2018b). It entails computing the integral of the product of a term in the budget, denoted here by x, with the time tendency, $\frac{\partial q_d}{\partial t}$, over a region A, and then dividing by the integral of the square of the tendency over the same region:

$$S_x(p) = \frac{\iint_A x \frac{\partial q_d}{\partial t}\,\mathrm{d}A}{\iint_A \left(\frac{\partial q_d}{\partial t}\right)^2 \mathrm{d}A}. \tag{8}$$

We have chosen the rectangular region 50°E to 110°E, 0° to 30°N as our region of interest (A). Note in our case $S_x(p)$ is a function of pressure, because our EPV budget is not a vertically-integrated quantity [unlike the column MSE budget, e.g., in the case of Adames and Ming (2018b)]. The results of this projection at each vertical level in our simulations are shown in Figure 6. Here it is quantitatively clear that anomalous horizontal advection of EPV is dominant in the mid-to-upper troposphere, while diabatic processes become more important in the lower troposphere, i.e. near 700 hPa. This is qualitatively consistent with the results of Boos et al. (2015). Vertical advection anomalies have a small negative contribution to the EPV tendency in the lower troposphere and a small positive contribution in the mid-to-upper troposphere; in general they tend to oppose the diabatic tendency throughout the atmosphere.

2) Linear versus nonlinear effects

Quantitatively, horizontal advection consists of two quadratic terms (one zonal and one meridional) in the budget. It is worth asking if these terms in the could potentially be treated as being linear in anomalies (either linear in a wind anomaly or linear in a EPV-gradient anomaly) or whether the anomalous horizontal advection tendency is nonlinear process (i.e. representing advection of EPV anomalies by the anomalous horizontal flow). At least for stronger storms Boos et al. (2015) suggest that nonlinear processes are at work.

We can look more closely at the horizontal advection term by breaking it down into zonal and meridional components, and performing a Reynolds decomposition on the terms:

$$-(\mathbf{u}\cdot\nabla q_d)' = -\frac{1}{a\cos\phi}\left(\overline{u}\,\frac{\partial q_d}{\partial\lambda}' + u'\overline{\frac{\partial q_d}{\partial\lambda}} + u'\,\frac{\partial q_d}{\partial\lambda}'\right) - \frac{1}{a}\left(\overline{v}\,\frac{\partial q_d}{\partial\phi}' + v'\overline{\frac{\partial q_d}{\partial\phi}} + v'\,\frac{\partial q_d}{\partial\phi}'\right). \quad (9)$$

Here we have taken the quadratic advection terms and broken them down into terms that are linear in anomalies and terms that are nonlinear in anomalies. The product of the means terms drop out (and are not shown), because they do not project onto the standardized regression index, which by definition has a mean of zero.

If we do this for each simulation, and project each term onto the total EPV tendency, we find, as was qualitatively shown in Figure 4(b), that advection of EPV anomalies by the mean zonal wind tends to work against the prevailing westward-propagating tendency of EPV in the lower-to-mid troposphere (the solid red line in Figure 7). Instead, the mechanism by which horizontal advection of EPV plays an important role in the westward-propagation of the storms is the advection of the JJAS mean EPV by the anomalous meridional winds (the dashed blue line in Figure 7). Because the anomalous meridional winds are cyclonic, they blow southward to the west of the storm (down the mean EPV gradient, bringing high mean EPV air from the north), and northward (up the mean EPV gradient, bringing low mean EPV air from the south) east of the storm, resulting in the dipole pattern seen in Figure 5(a). Nonlinear advection of the anomalous EPV by the anomalous meridional winds also makes a small positive contribution to the spatial pattern of the overall tendency of EPV in the lower troposphere, while nonlinear advection of the anomalous EPV by the anomalous zonal winds makes a small positive contribution in the upper troposphere. The other terms (advection of anomalous EPV by the mean meridional winds and advection of the JJAS mean EPV by the anomalous zonal winds) do not play an important role in the total horizontal advection term. The secondary role of nonlinear EPV advection in the budget suggests that beta drift is not a primary driver of propagation for the storms in our simulation.

d. Moisture vortex instability

Following the suggestion by Cohen and Boos (2016), Adames and Ming (2018a) developed a theory for the growth and propagation of monsoon low pressure systems within the moisture mode framework. The theory is based on using vertically-truncated versions of the momentum, thermodynamic, and moisture equations; in this context "vertically-truncated" means that the horizontal winds, temperature, geopotential, and specific humidity are projected onto basis functions consistent with a first-baroclinic mode vertical structure for the vertical velocity. This reduces the equations to a shallow water-like system, which is more amenable to analysis [e.g. as in Neelin and Zeng (2000), Haertel et al. (2008), or Adames and Kim (2015)]. In Adames and Ming (2018a), the truncated equations are linearized about a South Asian monsoon-season-like basic state, and through analysis of a dispersion relation, are shown to support a "moisture-vortex instability." The instability is associated with a partially in-phase relationship between precipitation anomalies (corresponding with upward vertical motion and convergence of low-level horizontal winds) and cyclonic (i.e. positive) vorticity anomalies. The precipitation anomalies, through their association with low-level convergence, result in a growing tendency for the vorticity anomalies through vortex-stretching Adames and Ming (2018a). Propagation of the wave in their framework is due to vortex stretching from moist convection in regions of isentropic ascent and horizontal moisture advection.

In terms of the primitive equations, moisture vortex instability theory depends on the advection of planetary vorticity, vortex stretching, meridional and vertical advection of the mean internal energy and moisture by the anomalous winds and latent heating due to precipitation (Adames and Ming 2018a). We can test whether these assumptions hold in the case of the storms in the LAND simulation by explicitly computing the anomalous vorticity, internal energy, and moisture budgets.

1) Vorticity budget

While nonlinear terms do make some contribution to the total horizontal advection term of the PV budget, the term's contribution as a whole between pressure levels 700 hPa and 200 hPa is reasonably well-approximated by the advection of the JJAS mean EPV by the anomalous meridional winds. This suggests that despite the fact that the mean zonal winds blow eastward at pressure levels with large PV anomalies (opposite to the direction of propagation of the storms), it might be possible to construct a linear model that would describe the storms' motion in our model. Adames and Ming (2018a) propose such a model; however their theory assumes that terms involving the mean state winds and/or wind shear in the horizontal momentum budget are negligible (in fact assuming that the anomalous horizontal momentum tendencies are approximated by the Coriolis force induced by the anomalous ageostrophic winds). This results in an equation for the anomalous vorticity tendency that only depends on vortex stretching associated with just the Coriolis parameter, and planetary vorticity advection by the anomalous meridional wind (i.e. the beta effect). It is clear in both reanalysis (Boos et al. 2015; Cohen and Boos 2016) and our simulations that the mean state climate is characterized by zonal winds on the order of $10\,\mathrm{m\,s^{-1}}$ and a vertical wind shear on the order of $1.0 \times 10^{-3}\,\mathrm{m\,s^{-1}\,Pa^{-1}}$ [Figure 1(h)]. It is worth investigating whether this mean state has a leading-order influence in the anomalous vorticity budget in our simulation, or whether it is in fact negligible.

A good place to start is the anomalous flux-form vorticity equation discussed in Boos et al. (2015):

$$\frac{\partial \zeta'}{\partial t} = -\left[\nabla \cdot (f+\zeta)\,\mathbf{u}\right]' - \nabla \cdot \left(\omega \hat{k} \times \frac{\partial \mathbf{u}}{\partial p}\right)'. \tag{10}$$

The only term in this budget that is included in the theory of Adames and Ming (2018a) is $-\nabla \cdot f\mathbf{u}$; this is the collective influence of vortex stretching and horizontal advection involving the planetary vorticity. All other terms, i.e. the collective influence of vortex stretching and horizontal advection involving the relative vorticity, $-\nabla \cdot \zeta \mathbf{u}$, and the collective influence of vertical vorticity advection and vortex tilting, $\nabla \cdot \left(\omega \hat{k} \times \frac{\partial \mathbf{u}}{\partial p}\right)$, are not included in their theory. Therefore, it is useful to view the spatial anomaly patterns from our simulation through this decomposition. For example, any influence of the background mean state, be it a mean meridional or mean vertical gradient in the zonal wind, would show up in the terms not containing the planetary vorticity, f.

We compute each term in Equation 10 explicitly from model output at each vertical level. The terms in the anomalous budget for a level in the upper troposphere (400 hPa) and a level in the lower troposphere (850 hPa), decomposed as described above, are shown in Figure 8. Panels (a) and (e) shows the anomalous time tendency of the relative vorticity. There we can see a dipole pattern oriented along an east-west axis, similar to what we see in the anomalous PV budget. In addition we can see that indeed the dominant term on the right hand side of Equation 10 is the term involving the planetary vorticity, which is what is assumed in Adames and Ming (2018a). Terms potentially involving the mean state winds are about an order of magnitude smaller at both 850 hPa and 400 hPa, and to some extent offset each other.

Again we can be more quantitative and show the importance of the terms across all pressure levels by performing projection analysis. The result is shown in Figure 9. There we can see that our budget closes nearly perfectly below about 500 hPa and only slightly diverges above, as evidenced by the dashed black line, representing the total of the terms on the right hand side of Equation 8 having a projection of about one at all pressure levels. In addition, we see quantitative evidence of the dominance of the planetary vorticity term [the red line in Figure 9], which indicates a spatial projection of over 0.5 below 300 hPa. It is only above 300 hPa anomoalous vortex stretching associated with the relative vorticity and/or anomalous relative vorticity advection, $-\nabla \cdot \zeta \mathbf{u}$, becomes of leading-order significance in the budget. The combined effects of anomalous vertical advection and vortex tilting do not project strongly onto the time tendency of relative vorticity anywhere in the troposphere.

2) COLUMN INTERNAL ENERGY BUDGET

In addition to the horizontal momentum equations, the model of Adames and Ming (2018a) depends on the vertically-integrated thermodynamic and moisture equations. The terms in the anomalous vertically-integrated thermodynamic equation can be written in the form (Neelin 2007):

$$C_p \frac{\partial \langle T \rangle'}{\partial t} = -C_p \langle \mathbf{u} \cdot \nabla T \rangle' - C_p \left\langle \omega \frac{\partial T}{\partial p} \right\rangle' - \left\langle \omega \frac{\partial \Phi}{\partial p} \right\rangle' + P' + F' + H'. \tag{11}$$

Here C_p is the specific heat of dry air at constant pressure; T is the temperature; $\Phi = gz$ is the geopotential; F is the net column radiation; and H is the sensible heat flux. The angle-brackets signify mass-weighted integration over the full column of the quantity inside:

$$\langle (\cdot) \rangle = \frac{1}{g} \int_0^{p_s} (\cdot)\, \mathrm{d}p. \tag{12}$$

We compute the full time-series of each term in this budget following the methods of Hill et al. (2017) in a two step procedure starting from the flux-form framing of the budget. First we compute the adjusted set of horizontal winds such that the budget closes with explicitly-computed values for the time tendency of column integrated temperature, column integrated product of the pressure velocity and vertical geopotential height gradient, and precipitation, net radiative, and surface sensible heat fluxes. We then explicitly compute the horizontal advection term in Equation 11 and finally compute the vertical advection term as a residual.

The vertical advection of temperature and geopotential offset each other to a large degree and are often grouped together as a vertical advection of dry static energy, $s = C_p T + \Phi$ (e.g. Neelin 2007; Adames and Ming 2018a). In addition, the net radiation and sensible heat terms in the anomalous budget make negligible contributions to the total; therefore we plot the anomalous terms of the following approximate form of the budget:

$$C_p \frac{\partial \langle T \rangle'}{\partial t} \approx -C_p \langle \mathbf{u} \cdot \nabla T \rangle' - \left\langle \omega \frac{\partial s}{\partial p} \right\rangle' + P', \tag{13}$$

which is exactly the same as Equation 11 with the exception of our ignoring of F' and H'.

The budget terms are plotted in Figure 10 along with contours indicating the values of anomalous vertically-integrated internal energy, $C_p \langle T \rangle'$. In Figure 10(a) we can see a negative anomaly in internal energy at the storm center, flanked by an anomalous negative internal energy tendency to the west and an anomalous positive internal energy tendency to the east; this dipole pattern in the tendency is consistent with the westward propagation of the negative internal energy anomaly at the storm center. The term on the right hand side of the budget that projects most strongly onto the time tendency is the sum of the vertical advection of dry static energy and the column-integrated latent heating associated with precipitation [Figure 10(c)]; overall this has a projection value of 2.31 on the tendency over the domain plotted. Horizontal advection of internal energy serves to damp this propagation tendency [Figure 10(b)]. Total horizontal advection has a projection value of -1.37; of this damping influence horizontal advection of mean internal energy by the anomalous meridional wind, $-\frac{C_p}{a}\left\langle v'\frac{\partial \overline{T}}{\partial \phi}\right\rangle'$, and horizontal advection of the anomalous internal energy by the anomalous meridional wind, $-\frac{C_p}{a}\left\langle v'\frac{\partial T'}{\partial \phi}\right\rangle'$, contribute -0.96 and -0.27 to the projection, respectively, indicating that the horizontal advection term is primarily due to the anomalous meridional wind acting on the mean temperature gradient (which is positive due to imposed the land-ocean contrast in heat capacity), with a smaller nonlinear addition. A full tabulation of the projections of each term in the decomposed internal energy budget can be found in Figure 11.

The picture here is largely consistent with the assumptions made in deriving the theory in Adames and Ming (2018a). There the anomalous radiative and sensible heating parts of the thermodynamic equation were neglected, and they are found to be quite small in our simulation. The terms retained in the anomalous thermodynamic budget in Adames and Ming (2018a) were the vertical advection of mean dry static energy by the anomalous pressure velocity, the column latent heating due to precipitation, and meridional advection of mean internal energy by the anomalous meridional wind. These are indeed the leading order terms in the anomalous thermodynamic budget in our simulation. We do, however, find a nontrivial contribution from the advection of the anomalous internal energy by the anomalous meridional wind, which without some closure would not be possible to represent in a linear model, such as that in Adames and Ming (2018a).

3) Column moisture budget

The anomalous column-integrated moisture budget can be written as Adames and Ming (2018b):

$$\frac{\partial \langle q_v \rangle'}{\partial t} = -\langle \mathbf{u}\cdot\nabla q_v\rangle' - \left\langle \omega \frac{\partial q_v}{\partial p}\right\rangle' - P' + E'. \tag{14}$$

Here q_v represents the specific humidity and P' and E' represent the precipitation and evaporation rates, respectively. The theory of Adames and Ming (2018a) assumes that of the terms in the anomalous budget in Equation 14, only the horizontal advection of the mean moisture by the anomalous meridional winds, vertical advection of moisture, and precipitation anomalies are important. It is worth verifying whether this is true in our simulation. We compute the full time-series of terms in the column integrated moisture budget in a two-step procedure. First we compute an adjusted set of horizontal winds at each vertical level following the methods of Hill et al. (2017) using the flux-form framing of the vertically-integrated budget to ensure the budget is balanced. We then use these adjusted horizontal winds to compute the horizontal advection term in Equation 14 explicitly, and compute the vertical advection term as a residual. We can then regress each of these time-series on the precipitation index to obtain anomalies at lag-day zero of a monsoon low pressure system event on the southeastern Indian coast.

We obtain the results shown in Figure 12. The time tendency anomaly pattern, panel (a), depicts an east-west-oriented dipole pattern, consistent with the westward propagation of the storms. The two largest terms on the right hand side of the budget are the vertical advection and precipitation terms; since they largely offset each other, as in Adames and Ming (2018b). we combine these into one term and refer to it as the "column moisture process." This aggregate term projects strongly onto the time tendency (with a projection value of 0.87 over the region plotted), though perhaps has a slightly northwestward orientation compared with the more westward orientation of the tendency itself. Horizontal advection plays a secondary role, and acts to turn the dipole orientation more toward the west (with a projection value of 0.24). The anomalous latent heat fluxes, panel (d), play a minor damping role, with a projection of -0.11. In the projection sense, these results are largely consistent with the results of Adames and Ming (2018b) in AM4; there the column moisture process term was dominant, with a minor positive contribution coming from horizontal advection, and a minor negative contribution coming from evaporation.

Similar to what we did with the internal energy budget, we can decompose the horizontal advection term into components due to the product of the mean winds and anomalous moisture gradients, products of the anomalous winds and the mean moisture gradients, and products of the anomalies. The result is shown in Figure 13. This allows us to determine the feasability of using a linear model of the column-integrated moisture equation. Here we find that the primary reason for the positive contribution of the horizontal advection of moisture to the westward-propagation tendency is the nonlinear component, with a total projection of 0.49 on the moisture tendency over the plotted domain, contributed roughly equally from the zonal and meridional components; in contrast the advection of the anomalous moisture anomalies by the mean winds provides a negative contribution, with a projection of -0.25 on the tendency over the plotted domain. In particular the negative projection is due primarily to the advection of moisture anomalies by the mean zonal wind. Terms involving mean horizontal moisture gradients are not found to be important, with a total projection of -0.001.

As assumed in Adames and Ming (2018a), the vertical advection of moisture and the loss of column moisture through precipitation play an important role in the moisture budget. That said, assumptions made regarding the horizontal advection of moisture in Adames and Ming (2018a) do not necessarily hold in our simulation. Adames and Ming (2018a) assume that advection of mean moisture by the anomalous meridional wind plays a leading-order role in the budget. We find this not to be the case. Rather, we find that advection of moisture anomalies by the mean eastward zonal wind, and nonlinear advection of moisture anomalies by the anomalous winds play leading-order roles. The significant positive projection of the nonlinear component of the horizontal advection is of particular interest, because it would not be possible to represent explicitly in a linear model.

6. Discussion and Conclusion

In this study we have completed a systematic anaylsis of low pressure systems in the Indian monsoon region in a heavily-idealized moist GCM. The low pressure systems found in our simulation share a number of characteristics with Indian monsoon low pressure systems observed in reality, or those simulated in comprehensive GCMs. For example precipitation anomalies in the Indian monsoon region in our simulation have a typical zonal scale of around zonal wavenumber 10, consistent with the scale seen in TRMM observations and AM4; the typical frequency of around $0.2\,\mathrm{d}^{-1}$ is consistent with that found in those datasets as well (Adames and Ming 2018b). In addition, we find that the vertical structure of potential vorticity anomalies associated with the low pressure systems simulated in our model shares an important qualitative feature with that found in reanalysis: the PV anomalies in the troposphere tilt slightly with the JJAS mean easterly zonal wind shear (Cohen and Boos 2016).

Aspects of the low pressure systems that differ slightly from those seen in reality are their propagation speed and direction. In our simulation, the storms propagate predominantly westward at speeds of over $6\,\mathrm{m\,s}^{-1}$; this is faster than storms seen in comprehensive GCMs or reanalysis. There are several possible explanations for this difference. Two of these arise from Rossby wave theory. From inspection of Fig. 3 it is possible that these waves are of slightly larger scale than the low pressure systems simulated in AM4 and observed in reanalysis. Because these systems occur at a lower latitude than in the aforementioned datasets, the Rossby radius of deformation is smaller, which would cause these systems to exhibit faster eastward propagation (see Eq. 22a in Adames and Ming 2018a) . We find very little northward component to the propagation direction, which is different than at least reanalysis Boos et al. (2015); in GFDL's AM4 model, storms propagated predominantly westward as well. It is possible that the northward component of propagation is largely a result of nonlinear beta drift, which is characteristic of the stronger storms that were analyzed by Boos et al. (2015).

The movement of the weak disturbances in our LAND simulation can largely be explained through linearized versions of the primitive equations, rather than beta drift, as was the case for monsoon depressions analyzed in reanalysis in Boos et al. (2015). The main exception is in the horizontal advection of moisture, where nonlinear moisture advection plays a nontrivial role. In addition, the fact that the storms move rapidly westward in the absence of any topographical features suggests that aid provided by a topographically-induced image vortex (e.g., as discussed in Hunt and Parker 2016) may not be not necessary. The possibility of an explanation via a linear model (like the one discussed in Adames and Ming 2018a) could motivate further sensitivity studies in a framework like this, to test whether properties of the mean state, like the meridional temperature or moisture gradient, could influence properties of the low pressure systems, like the phase speed.

In addition, while the work we have done here demonstrates that somewhat realistic monsoon low pressure system-like disturbances can be simulated with simplified model physics and boundary conditions, it does not rule out that even further idealizations could be made. We intentionally used realistic continental geometry and a hydrology model to limit evaporation over land, as to remove those as possible reasons for too unrealistic a mean climate to support MLPSs; however, when moving to try and systematically change the mean state as suggested above, it might be valuable to use a simpler land setup, perhaps without complex land shapes and a bucket hydrology scheme, closer maybe to the "moist land" simulations with a rectangular continent in Zhou and Xie (2018).

Acknowledgments. We thank Spencer Hill for helpful discussions regarding procedures for computing closed vertically-integrated tracer budgets. S.K.C. was supported by a National Defense Science and Engineering Fellowship. Á.F.A. was supported by the University of Michigan's startup package.

References

Adames, A. F., and D. Kim, 2015: The MJO as a Dispersive, Convectively Coupled Moisture Wave: Theory and Observations. *Journal of the Atmospheric Sciences*, **73 (3)**, 913–941, doi: 10.1175/JAS-D-15-0170.1.

Adames, A. F., and Y. Ming, 2018a: Interactions between Water Vapor and Potential Vorticity in Synoptic-Scale Monsoonal Disturbances: Moisture Vortex Instability. *Journal of the Atmospheric Sciences*, **75 (6)**, 2083–2106, doi:10.1175/JAS-D-17-0310.1.

Adames, A. F., and Y. Ming, 2018b: Moisture and moist static energy budgets of South Asian monsoon low pressure systems in GFDL AM4.0. *Journal of the Atmospheric Sciences*, doi: 10.1175/JAS-D-17-0309.1.

Adames, A. F., and J. M. Wallace, 2014: Three-Dimensional Structure and Evolution of the MJO and Its Relation to the Mean Flow. *Journal of the Atmospheric Sciences*, **71 (6)**, 2007–2026, doi:10.1175/JAS-D-13-0254.1.

Ajayamohan, R. S., W. J. Merryfield, and V. V. Kharin, 2010: Increasing Trend of Synoptic Activity and Its Relationship with Extreme Rain Events over Central India. *Journal of Climate*, **23 (4)**, 1004–1013, doi:10.1175/2009JCLI2918.1.

Andersen, J. A., and Z. Kuang, 2011: Moist Static Energy Budget of MJO-like Disturbances in the Atmosphere of a Zonally Symmetric Aquaplanet. *Journal of Climate*, **25 (8)**, 2782–2804, doi:10.1175/JCLI-D-11-00168.1.

Becker, T., and B. Stevens, 2014: Climate and climate sensitivity to changing CO2 on an idealized land planet. *Journal of Advances in Modeling Earth Systems*, **6 (4)**, 1205–1223, doi:10.1002/2014MS000369.

Blackburn, M., and Coauthors, 2013: The Aqua-Planet Experiment (APE): CONTROL SST Simulation. *Journal of the Meteorological Society of Japan. Ser. II*, **91A**, 17–56, doi:10.2151/jmsj.2013-A02.

Bluestein, H., 1992: *Synoptic-Dynamic Meteorology in Midlatitudes: Principles of Kinematics and Dynamics*, Vol. 1. Oxford University Press.

Boos, W. R., J. V. Hurley, and V. S. Murthy, 2015: Adiabatic westward drift of Indian monsoon depressions. *Quarterly Journal of the Royal Meteorological Society*, **141 (689)**, 1035–1048, doi:10.1002/qj.2454.

Boville, B. A., 1986: Wave–Mean Flow Interactions in a General Circulation Model of the Troposphere and Stratosphere. *Journal of the Atmospheric Sciences*, **43 (16)**, 1711–1725, doi:10.1175/1520-0469(1986)043⟨1711:WFIIAG⟩2.0.CO;2.

Byrne, M. P., and P. A. O'Gorman, 2012: Land–Ocean Warming Contrast over a Wide Range of Climates: Convective Quasi-Equilibrium Theory and Idealized Simulations. *Journal of Climate*, **26 (12)**, 4000–4016, doi:10.1175/JCLI-D-12-00262.1.

Clark, S. K., Y. Ming, I. M. Held, and P. J. Phillipps, 2018: The Role of the Water Vapor Feedback in the ITCZ Response to Hemispherically Asymmetric Forcings. *Journal of Climate*, **31 (9)**, 3659–3678, doi:10.1175/JCLI-D-17-0723.1.

Cohen, N. Y., and W. R. Boos, 2016: Perspectives on Moist Baroclinic Instability: Implications for the Growth of Monsoon Depressions. *Journal of the Atmospheric Sciences*, **73 (4)**, 1767–1788, doi:10.1175/JAS-D-15-0254.1.

Cronin, T. W., K. A. Emanuel, and P. Molnar, 2015: Island precipitation enhancement and the diurnal cycle in radiative-convective equilibrium. *Quarterly Journal of the Royal Meteorological Society*, **141 (689)**, 1017–1034, doi:10.1002/qj.2443.

Dee, D. P., and Coauthors, 2011: The ERA-Interim reanalysis: Configuration and performance of the data assimilation system. *Quarterly Journal of the Royal Meteorological Society*, **137 (656)**, 553–597, doi:10.1002/qj.828.

Diaz, M., and W. R. Boos, 2018: Barotropic Growth of Monsoon Depressions. *Quarterly Journal of the Royal Meteorological Society*, **0 (ja)**, doi:10.1002/qj.3467.

Ditchek, S. D., W. R. Boos, S. J. Camargo, and M. K. Tippett, 2016: A Genesis Index for Monsoon Disturbances. *Journal of Climate*, **29 (14)**, 5189–5203, doi:10.1175/JCLI-D-15-0704.1.

Fiorino, M., and R. L. Elsberry, 1988: Some Aspects of Vortex Structure Related to Tropical Cyclone Motion. *Journal of the Atmospheric Sciences*, **46 (7)**, 975–990, doi:10.1175/1520-0469(1989)046⟨0975:SAOVSR⟩2.0.CO;2.

Frierson, D. M. W., 2007: The Dynamics of Idealized Convection Schemes and Their Effect on the Zonally Averaged Tropical Circulation. *Journal of the Atmospheric Sciences*, **64 (6)**, 1959–1976, doi:10.1175/JAS3935.1.

Frierson, D. M. W., I. M. Held, and P. Zurita-Gotor, 2006: A Gray-Radiation Aquaplanet Moist GCM. Part I: Static Stability and Eddy Scale. *Journal of the Atmospheric Sciences*, **63 (10)**, 2548–2566, doi:10.1175/JAS3753.1.

Frierson, D. M. W., I. M. Held, and P. Zurita-Gotor, 2007: A Gray-Radiation Aquaplanet Moist GCM. Part II: Energy Transports in Altered Climates. *Journal of the Atmospheric Sciences*, **64 (5)**, 1680–1693, doi:10.1175/JAS3913.1.

Geen, R., F. H. Lambert, and G. K. Vallis, 2017: Regime Change Behavior during Asian Monsoon Onset. *Journal of Climate*, **31 (8)**, 3327–3348, doi:10.1175/JCLI-D-17-0118.1.

Godbole, R. V., 1977: The composite structure of the monsoon depression. *Tellus*, **29 (1)**, 25–40, doi:10.1111/j.2153-3490.1977.tb00706.x.

Haertel, P. T., G. N. Kiladis, A. Denno, and T. M. Rickenbach, 2008: Vertical-Mode Decompositions of 2-Day Waves and the Madden–Julian Oscillation. *Journal of the Atmospheric Sciences*, **65 (3)**, 813–833, doi:10.1175/2007JAS2314.1.

Hendon, H. H., and M. C. Wheeler, 2008: Some Space–Time Spectral Analyses of Tropical Convection and Planetary-Scale Waves. *Journal of the Atmospheric Sciences*, **65 (9)**, 2936–2948, doi:10.1175/2008JAS2675.1.

Hill, S. A., Y. Ming, I. M. Held, and M. Zhao, 2017: A Moist Static Energy Budget–Based Analysis of the Sahel Rainfall Response to Uniform Oceanic Warming. *Journal of Climate*, **30 (15)**, 5637–5660, doi:10.1175/JCLI-D-16-0785.1.

Huffman, G. J., and Coauthors, 2007: The TRMM Multisatellite Precipitation Analysis (TMPA): Quasi-Global, Multiyear, Combined-Sensor Precipitation Estimates at Fine Scales. *Journal of Hydrometeorology*, **8 (1)**, 38–55, doi:10.1175/JHM560.1.

Hunt, K. M., and A. G. Turner, 2017: The effect of horizontal resolution on Indian monsoon depressions in the Met Office NWP model. *Quarterly Journal of the Royal Meteorological Society*, **143 (705)**, 1756–1771, doi:10.1002/qj.3030.

Hunt, K. M. R., and D. J. Parker, 2016: The movement of Indian monsoon depressions by interaction with image vortices near the Himalayan wall. *Quarterly Journal of the Royal Meteorological Society*, **142 (698)**, 2224–2229, doi:10.1002/qj.2812.

Hunt, K. M. R., A. G. Turner, P. M. Inness, D. E. Parker, and R. C. Levine, 2016a: On the Structure and Dynamics of Indian Monsoon Depressions. *Monthly Weather Review*, **144 (9)**, 3391–3416, doi:10.1175/MWR-D-15-0138.1.

Hunt, K. M. R., A. G. Turner, and D. E. Parker, 2016b: The spatiotemporal structure of precipitation in Indian monsoon depressions. *Quarterly Journal of the Royal Meteorological Society*, **142 (701)**, 3195–3210, doi:10.1002/qj.2901.

Hurley, J. V., and W. R. Boos, 2015: A global climatology of monsoon low-pressure systems. *Quarterly Journal of the Royal Meteorological Society*, **141 (689)**, 1049–1064, doi:10.1002/qj.2447.

Jablonowski, C., and D. L. Williamson, 2011: The Pros and Cons of Diffusion, Filters and Fixers in Atmospheric General Circulation Models. *Numerical Techniques for Global Atmospheric Models*, P. Lauritzen, C. Jablonowski, M. Taylor, and R. Nair, Eds., Lecture Notes in Computational Science and Engineering, Springer Berlin Heidelberg, Berlin, Heidelberg, 381–493, doi:10.1007/978-3-642-11640-7_13.

Jucker, M., and E. P. Gerber, 2017: Untangling the Annual Cycle of the Tropical Tropopause Layer with an Idealized Moist Model. *Journal of Climate*, **30 (18)**, 7339–7358, doi:10.1175/

JCLI-D-17-0127.1.

Krishnamurti, T. N., M. Kanamitsu, R. Godbole, C.-B. Chang, F. Carr, and J. H. Chow, 1976a: Study of a Monsoon Depression (II), Dynamical Structure. *Journal of the Meteorological Society of Japan. Ser. II*, **54 (4)**, 208–225, doi:10.2151/jmsj1965.54.4_208.

Krishnamurti, T. N., A. Martin, R. Krishnamurti, A. Simon, A. Thomas, and V. Kumar, 2013: Impacts of enhanced CCN on the organization of convection and recent reduced counts of monsoon depressions. *Climate Dynamics*, **41 (1)**, 117–134, doi:10.1007/s00382-012-1638-z.

Krishnamurti, T. N., J. Molinari, and H. L. Pan, 1976b: Numerical Simulation of the Somali Jet. *Journal of the Atmospheric Sciences*, **33 (12)**, 2350–2362, doi:10.1175/1520-0469(1976)033⟨2350:NSOTSJ⟩2.0.CO;2.

Lindberg, C., and A. J. Broccoli, 1996: Representation of Topography in Spectral Climate Models and Its Effect on Simulated Precipitation. *Journal of Climate*, **9 (11)**, 2641–2659, doi:10.1175/1520-0442(1996)009⟨2641:ROTISC⟩2.0.CO;2.

Lindzen, R. S., B. Farrell, and A. J. Rosenthal, 1983: Absolute Barotropic Instability and Monsoon Depressions. *Journal of the Atmospheric Sciences*, **40 (5)**, 1178–1184, doi:10.1175/1520-0469(1983)040⟨1178:ABIAMD⟩2.0.CO;2.

Lutsko, N. J., 2017: The Response of an Idealized Atmosphere to Localized Tropical Heating: Superrotation and the Breakdown of Linear Theory. *Journal of the Atmospheric Sciences*, **75 (1)**, 3–20, doi:10.1175/JAS-D-17-0192.1.

Mak, M., 1983: A Moist Baroclinic Model for Monsoonal Mid-Tropospheric Cyclogenesis. *Journal of the Atmospheric Sciences*, **40 (5)**, 1154–1162, doi:10.1175/1520-0469(1983)040⟨1154:AMBMFM⟩2.0.CO;2.

Manabe, S., 1969: Climate and the ocean circulation. *Monthly Weather Review*, **97 (11)**, 739–774, doi:10.1175/1520-0493(1969)097⟨0739:CATOC⟩2.3.CO;2.

Maroon, E. A., and D. M. W. Frierson, 2016: The impact of a continent's longitudinal extent on tropical precipitation. *Geophysical Research Letters*, **43 (22)**, 11,921–11,929, doi:10.1002/2016GL071518.

Maroon, E. A., D. M. W. Frierson, S. M. Kang, and J. Scheff, 2016: The Precipitation Response to an Idealized Subtropical Continent. *Journal of Climate*, **29 (12)**, 4543–4564, doi:10.1175/JCLI-D-15-0616.1.

Masunaga, H., T. S. L'Ecuyer, and C. D. Kummerow, 2006: The Madden–Julian Oscillation Recorded in Early Observations from the Tropical Rainfall Measuring Mission (TRMM). *Journal of the Atmospheric Sciences*, **63 (11)**, 2777–2794, doi:10.1175/JAS3783.1.

Merlis, T. M., T. Schneider, S. Bordoni, and I. Eisenman, 2012a: Hadley Circulation Response to Orbital Precession. Part I: Aquaplanets. *Journal of Climate*, **26 (3)**, 740–753, doi:10.1175/JCLI-D-11-00716.1.

Merlis, T. M., T. Schneider, S. Bordoni, and I. Eisenman, 2012b: Hadley Circulation Response to Orbital Precession. Part II: Subtropical Continent. *Journal of Climate*, **26 (3)**, 754–771, doi:10.1175/JCLI-D-12-00149.1.

Mishra, S. K., and P. S. Salvekar, 1980: Role of Baroclinic Instability in the Development of Monsoon Disturbances. *Journal of the Atmospheric Sciences*, **37 (2)**, 383–394, doi:10.1175/1520-0469(1980)037⟨0383:ROBIIT⟩2.0.CO;2.

Moorthi, S., and A. Arakawa, 1985: Baroclinic Instability with Cumulus Heating. *Journal of the Atmospheric Sciences*, **42 (19)**, 2007–2031, doi:10.1175/1520-0469(1985)042⟨2007:BIWCH⟩2.0.CO;2.

Neelin, J. D., 2007: Moist dynamics of tropical convection zones in monsoons, teleconnections and global warming. *The Global Circulation of the Atmosphere*, Princeton University Press, 267–302.

Neelin, J. D., and N. Zeng, 2000: A Quasi-Equilibrium Tropical Circulation Model—Formulation. *Journal of the Atmospheric Sciences*, **57 (11)**, 1741–1766, doi:10.1175/1520-0469(2000)057⟨1741:AQETCM⟩2.0.CO;2.

O'Gorman, P. A., and T. Schneider, 2008: The Hydrological Cycle over a Wide Range of Climates Simulated with an Idealized GCM. *Journal of Climate*, **21 (15)**, 3815–3832, doi:10.1175/2007JCLI2065.1.

Sandeep, S., R. S. Ajayamohan, W. R. Boos, T. P. Sabin, and V. Praveen, 2018: Decline and poleward shift in Indian summer monsoon synoptic activity in a warming climate. *Proceedings of the National Academy of Sciences*, **115 (11)**, 2681–2686, doi:10.1073/pnas.1709031115.

Seager, R., and N. Henderson, 2013: Diagnostic Computation of Moisture Budgets in the ERA-Interim Reanalysis with Reference to Analysis of CMIP-Archived Atmospheric Model Data. *Journal of Climate*, **26 (20)**, 7876–7901, doi:10.1175/JCLI-D-13-00018.1.

Shukla, J., 1977: Barotropic-Baroclinic instability of mean zonal wind during summer monsoon. *pure and applied geophysics*, **115 (5-6)**, 1449–1461, doi:10.1007/BF00874418.

Shukla, J., 1978: CISK-Barotropic-Baroclinic Instability and the Growth of Monsoon Depressions. *Journal of the Atmospheric Sciences*, **35 (3)**, 495–508, doi:10.1175/1520-0469(1978)035⟨0495:CBBIAT⟩2.0.CO;2.

Sikka, D. R., 1977: Some aspects of the life history, structure and movement of monsoon depressions. *pure and applied geophysics*, **115 (5-6)**, 1501–1529, doi:10.1007/BF00874421.

Vallis, G. K., and Coauthors, 2018: Isca, v1.0: A framework for the global modelling of the atmospheres of Earth and other planets at varying levels of complexity. *Geosci. Model Dev.*, **11 (3)**, 843–859, doi:10.5194/gmd-11-843-2018.

Voigt, A., and Coauthors, 2016: The tropical rain belts with an annual cycle and a continent model intercomparison project: TRACMIP. *Journal of Advances in Modeling Earth Systems*, n/a–n/a, doi:10.1002/2016MS000748.

Wang, Y., and G. J. Holland, 1996: The Beta Drift of Baroclinic Vortices. Part II: Diabatic Vortices. *Journal of the Atmospheric Sciences*, **53 (24)**, 3737–3756, doi:10.1175/1520-0469(1996)053⟨3737:TBDOBV⟩2.0.CO;2.

Welch, P., 1967: The use of fast Fourier transform for the estimation of power spectra: A method based on time averaging over short, modified periodograms. *IEEE Transactions on Audio and Electroacoustics*, **15 (2)**, 70–73, doi:10.1109/TAU.1967.1161901.

Wheeler, M., and G. N. Kiladis, 1999: Convectively Coupled Equatorial Waves: Analysis of Clouds and Temperature in the Wavenumber–Frequency Domain. *Journal of the Atmospheric Sciences*, **56 (3)**, 374–399, doi:10.1175/1520-0469(1999)056⟨0374:CCEWAO⟩2.0.CO;2.

Xie, S.-P., and N. Saiki, 1999: Abrupt Onset and Slow Seasonal Evolution of Summer Monsoon in an Idealized GCM Simulation. *Journal of the Meteorological Society of Japan. Ser. II*, **77 (4)**, 949–968, doi:https://doi.org/10.2151/jmsj1965.77.4_949.

Zhou, W., and S.-P. Xie, 2018: A Hierarchy of Idealized Monsoons in an Intermediate GCM. *Journal of Climate*, **31 (22)**, 9021–9036, doi:10.1175/JCLI-D-18-0084.1.

LIST OF FIGURES

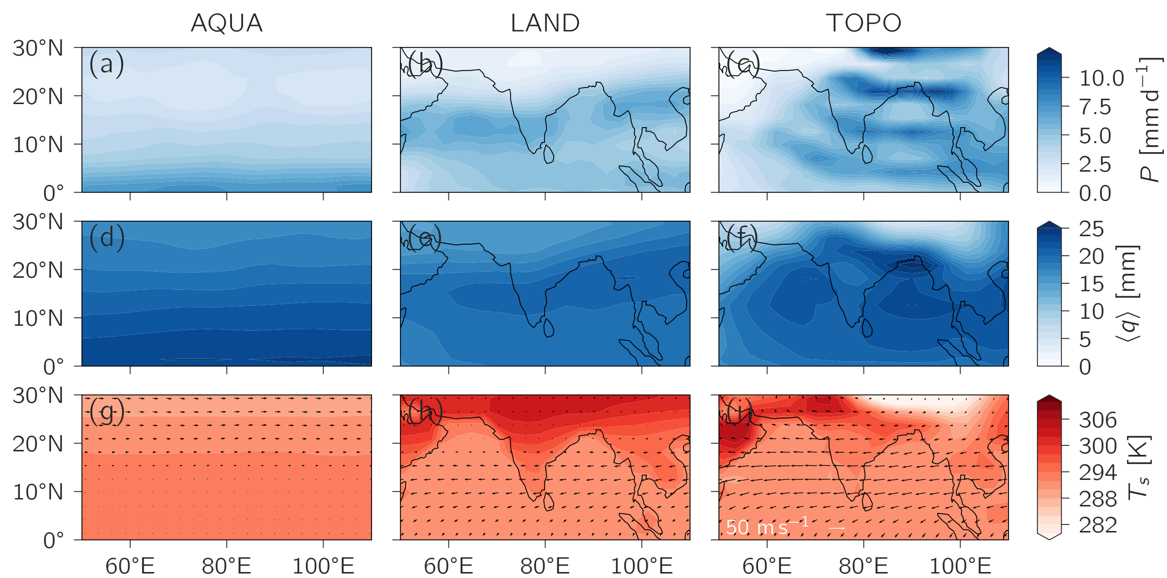

FIG. 1. JJAS mean precipitation rate (a)-(c); JJAS mean column integrated water vapor (d)-(f); and JJAS mean surface temperature (colors) (g)-(i). Vectors in (g)-(i) represent the direction and magnitude of the difference in horizontal wind between 200 hPa and 850 hPa. The columns represent data from the AQUA, LAND, and TOPO cases, respectively.

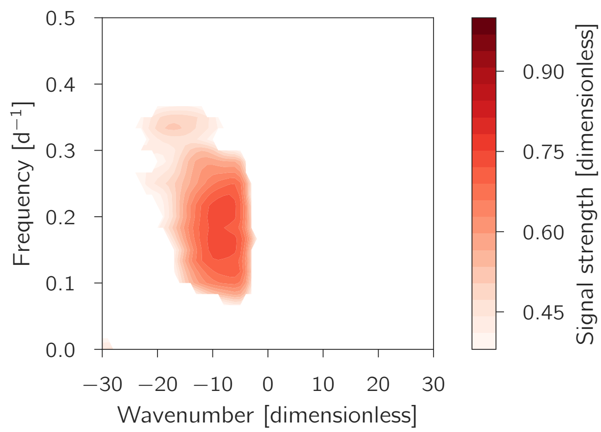

FIG. 2. Frequency-wavenumber spectrum of the JJAS precipitation rate in the LAND simulation. All values below the 99% threshold for statistical significance (0.38) are masked.

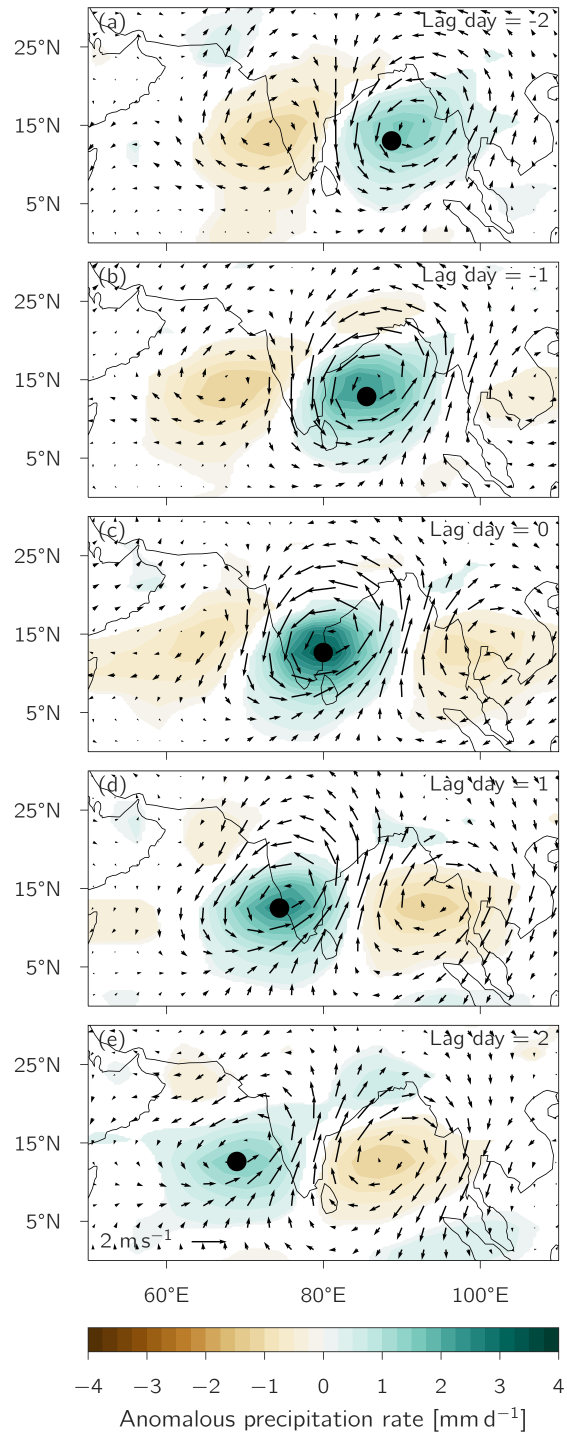

1019 FIG. 3. Precipitation rate (colors) and 850 hPa horizontal winds lag-regressed onto the precipitation index
1020 defined in Section ? for the LAND simulation. Only precipitation anomalies statistically-significant at the 99%
1021 level are plotted. The lag day is indicated in the upper right portion of each row (time moves forward downward).
1022 In all panels, the centroid of the positive precipitation anomalies is indicated by the filled black dot.

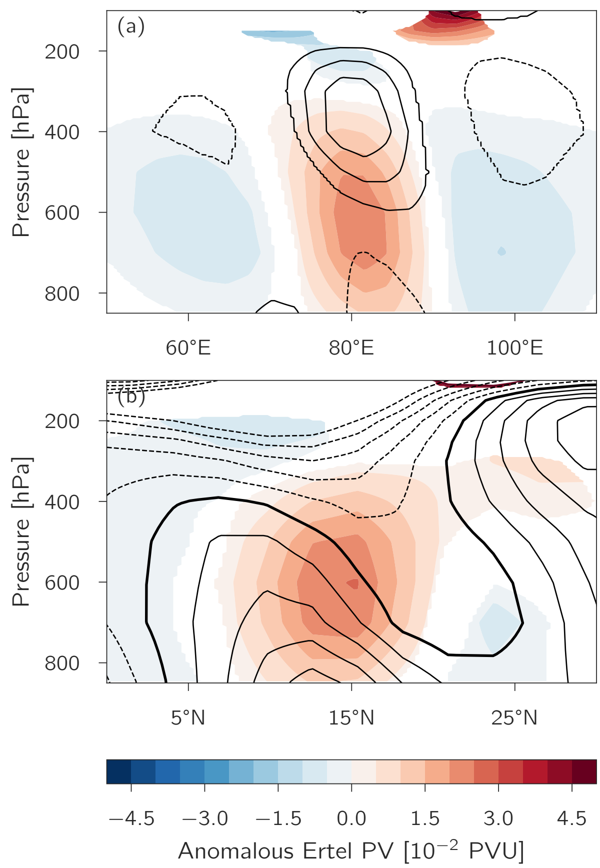

FIG. 4. Zonal cross section of EPV (colors) and temperature (lines) anomalies in the LAND experiment (a); Meridional cross section of Ertel EPV anomalies (colors) and JJAS mean zonal wind (lines) (b). Only statistically-significant anomalies at the 99% level are shown. The dashed contours represent negative values, while the solid contours represent positive values. In (b) the bold contour is the zero line. The first temperature anomaly contour in (a) greater than (less than) zero is 0.06 K (−0.06 K); with the exception of the omission of the zero contour, temperature anomaly contours are separated by 0.06 K. The zonal wind contours in (b) are separated by $2\,\mathrm{m\,s^{-1}}$.

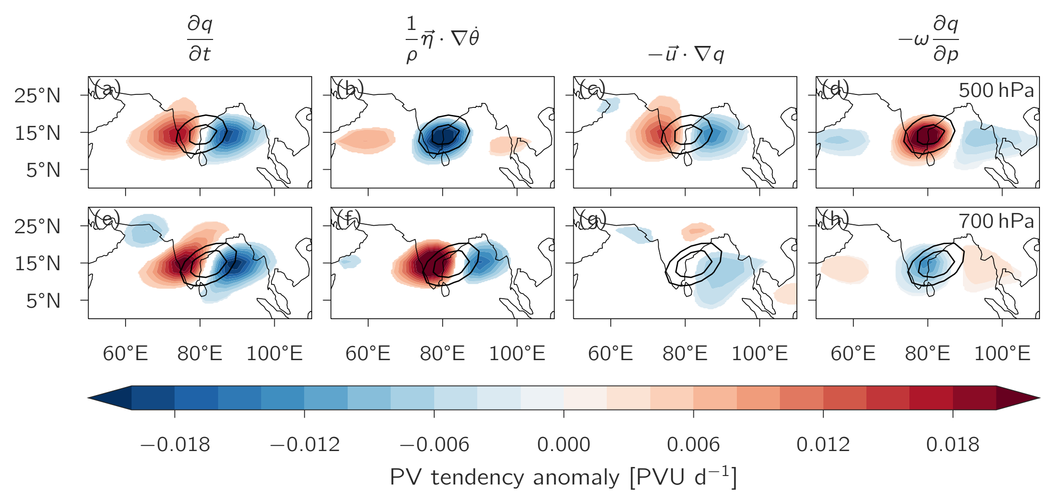

1030 FIG. 5. Anomalous terms in the Ertel PV budget in the LAND simulation at 500 hPa (row one) 700 hPa
1031 (row two). The black contours represent isolines of PV anomalies of 0.01 PVU and 0.02 PVU. Only values
1032 statistically-significant at the 99% level are shown.

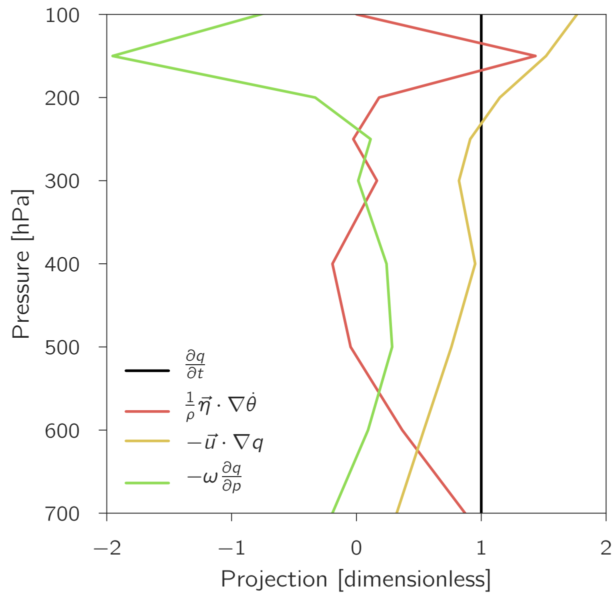

1033 FIG. 6. Projection of EPV budget terms on $\frac{\partial q_d}{\partial t}$ in the LAND simulation. The sum of the colored lines results
1034 in the black line, the projection of the tendency of EPV onto itself.

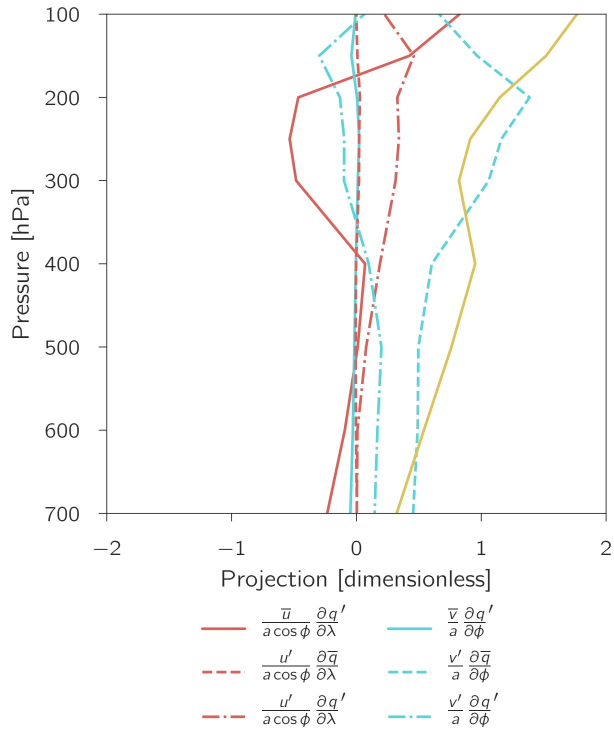

FIG. 7. Projection of terms comprising the total horizontal advection anomaly (see Equation 9) on $\frac{\partial q_d}{\partial t}$ in the LAND simulation. The sum of the red and blue lines results in the yellow line, the projection of the total anomalous horizontal advection term, $-(\mathbf{u}\cdot\nabla q_d)'$, onto the total anomalous time tendency of PV.

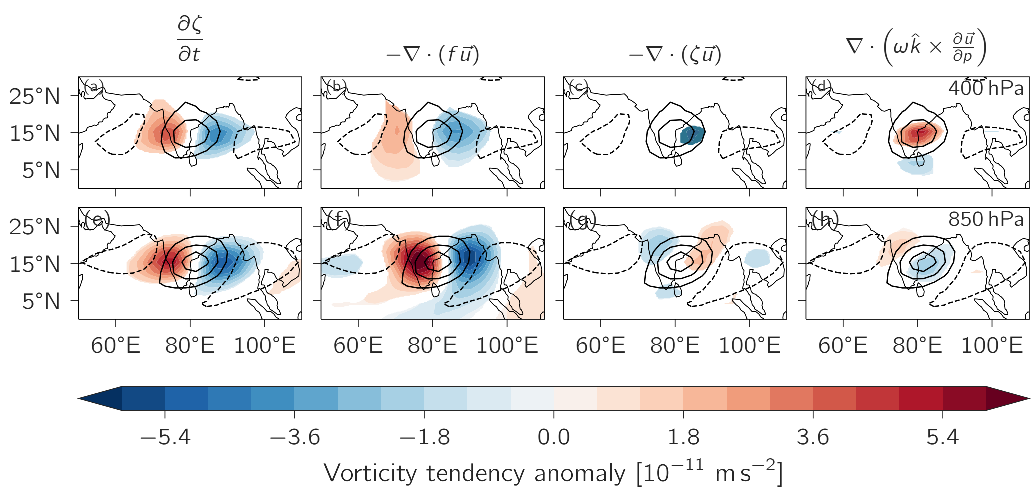

1038 FIG. 8. Terms in the anomalous vorticity budget (colors) at 400 hPa (row one) and 850 hPa (row two). Only values statistically-significant at the 99% level are shown. Contours represent relative vorticity anomalies, ζ'; contour levels start at $\pm 1.0 \times 10^{-6}$ s^{-1} and are separated by intervals of 2.0×10^{-6} s^{-1}. Dashed contours represent negative anomalies, while solid contours represent positive anomalies.

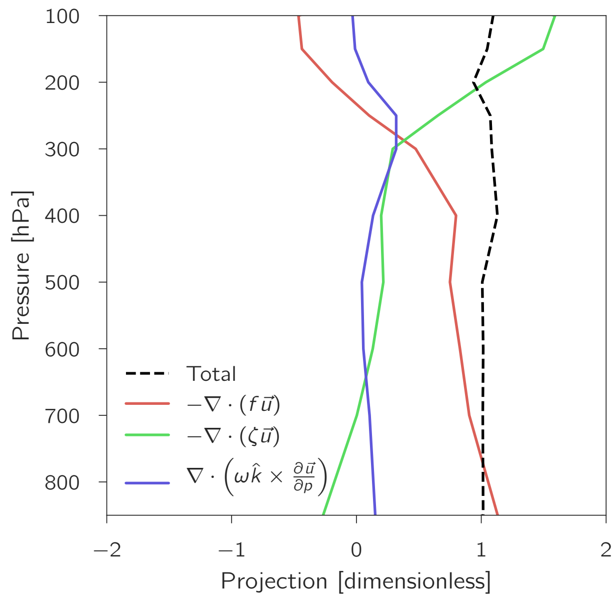

FIG. 9. Projection of vorticity budget terms on the time tendency of the relative vorticity.

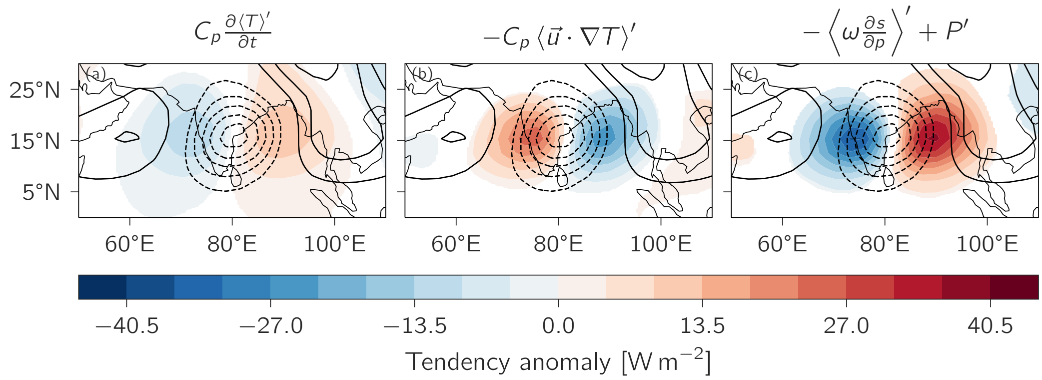

FIG. 10. Terms in the anomalous thermodynamic budget (colors) with anomalous column integrated internal energy, $C_p \langle T \rangle'$, overlaid (contours). Only budget values statistically-significant at a 99% level are shown. Negative contours are dashed; positive contours are solid. With the exception of the omission of the zero contour, contours are separated by an interval of 2.5×10^5 J kg^{-1}.

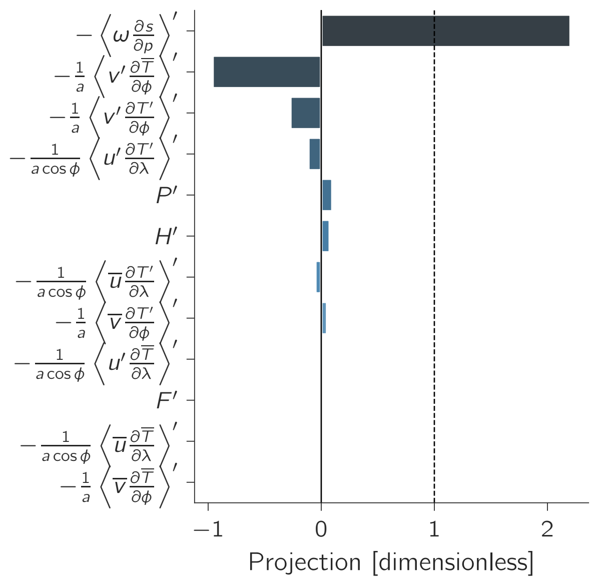

FIG. 11. Projection of the terms on the right hand side of the column-integrated internal energy budget sorted in descending order by absolute value. The horizontal advection term is comprehensively decomposed into linear and nonlinear components. The sum of the components adds exactly to 1.0.

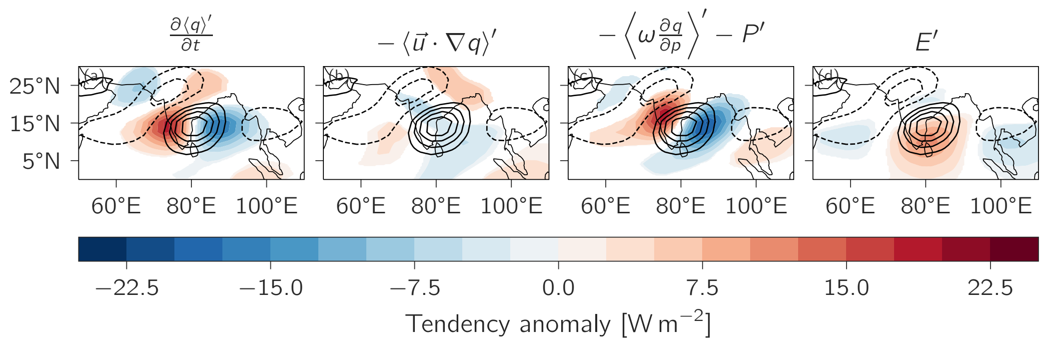

FIG. 12. Terms in the anomalous moisture budget, scaled by the latent heat of vaporization, $L_v = 2.5 \times 10^6\,\mathrm{J\,kg^{-1}}$, to place values in units of $\mathrm{W\,m^{-2}}$ (colors). Only tendency anomalies statistically-significant at the 99% level are shown. Contours represent column integrated moisture anomalies also scaled by the latent heat of vaporization, L_v. Negative contours are dashed; positive contours are solid. With the exception of the omission of the zero contour, contours are separated by intervals of $4.0 \times 10^5\,\mathrm{J\,m^{-2}}$.

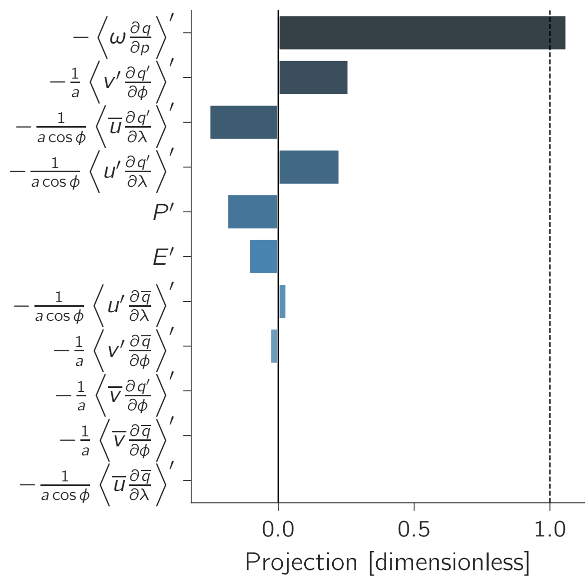

FIG. 13. Projection of the terms on the right hand side of the column-integrated moisture budget sorted in descending order by absolute value. The horizontal advection term is comprehensively decomposed into linear and nonlinear components. The sum of the components adds exactly to 1.0.